ACS APPLIED MATERIALS & INTERFACES

Research Article

www.acsami.org

Wire-in-Tube IrO_x Architectures: Alternative Label-Free Immunosensor for Amperometric Immunoassay toward α-Fetoprotein

Qingling Li, Dali Liu, Lin Xu,* Ruiqing Xing, Wei Liu, Kuang Sheng, and Hongwei Song*

State Key Laboratory on Integrated Optoelectronics, College of Electronic Science and Engineering, Jilin University, 2699 Qianjin Street, Changchun, 130012, P. R. China

Supporting Information

ABSTRACT: A sensitive, label-free immunosensor based on iridium oxide (IrO_x, $0 \le x \le 2$) nanofibers, which were synthesized through a simple one-spinneret electrospinning method, was first developed for immunoassay of the cancer biomarker α-fetoprotein (AFP). The specific wire-in-tube nanostructure could be obtained and the composition of IrO_x nanofibers also could be controlled through changing the annealing temperature. The unique structure and properties of IrO_x nanofibers obtained at 500 °C not only led to increased electrode surface area and accelerated electron transfer kinetics but also could provide a highly stable matrix for the convenient conjugation of biomolecules together with chitosan (CS). The good electrochemical properties of the IrO_x-nanofiber-modified immunosensor allowed one to detect AFP over a wide concentration range from 0.05 to 150 ng/mL, with a detection limit of 20 pg/mL. The proposed immunosensor also has been used to determine AFP in human serum with satisfactory results. The present protocol was shown to be quite promising for clinical screening of cancer biomarkers and point-of-care diagnostics applications.

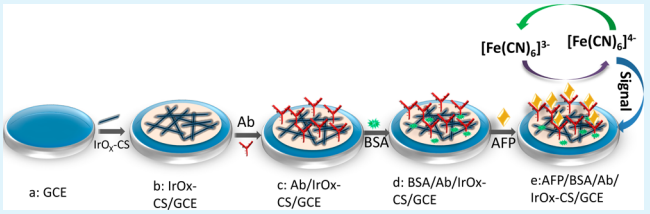

KEYWORDS: *IrO_x, electrospinning, wire-in-tube nanostructure, electrochemical immunosensor, label-free, α-fetoprotein*

1. INTRODUCTION

α-Fetoprotein (AFP) is the most reliable clinical tumor marker for hepatocellular carcinoma screening and tracking. Specifically, the analysis of AFP also offers great opportunities to understand the disease progression and to monitor patient responses to therapy methods.[1,2] Generally, the concentration of AFP is below 25 ng/mL in healthy human serum; otherwise, a rise of serum AFP level is routinely taken as an abnormality in adults.[3] Therefore, many novel technologies were developed and applied to detect elevated AFP concentration.[4−7] Recently, electrochemical immunosensors have gained increasing attention and are considered to be one of the most promising methods in the quantitative detection of AFP because of their specific advantages, such as low cost, excellent detection limits, fast response, and easy handling.[8,9]

For the construction of an excellent electrochemical immunosensor, especially for a label-free electrochemical immunosensor, one key factor is the efficient and effective immobilization of biomolecules onto the electrode surface. Therefore, the electrode materials should have improved conductivity in order to assist the electron transfer and also provide a large surface area to immobilize more antibodies, as well as good biocompatibility and stability. Up to now, the noble-metal- and graphene-based label-free AFP immunosensors have been widely applied to the electrochemical biosensor due to their good conductivity.[10] Actually, besides the appropriate electrode material, it is known that the nanostructure also has a large influence on the physical and chemical properties of the nanomaterial. Among various nanostructures, one-dimensional (1D) materials synthesized by electrospinning are very suitable as a building block of an electrochemical biosensor,[11−13] typically having diameters ranging from tens of nanometers up to few micrometers and lengths up to several centimeters and also potentially accelerating the electron transfer.[14−16] However, it is still a challenge to obtain noble-metal and graphene nanofibers through electrospinning, due to their poor thermostability.

Recently, iridium oxide (IrO_x), which has metal-like conductivity and a resistance of ∼50 μΩ cm in bulk, has attracted much attention due to its excellent performance in electrochemical sensors.[17,18] Moreover, its especially superior chemical and thermal stability also make it much easier to control the structure of IrO_x. Kim et al. reported the high electroactivity of IrO_x nanofibers synthesized by simple electrospinning and applied in the highly selective and sensitive amperometric detection of ascorbic acid.[19] Zhao et al. used template-assisted deposition and etching strategy to prepare IrO_2 nanotube arrays on indium−tin oxide (ITO) substrates, which enhanced their electrocatalytic activity toward oxygen evolution reaction.[20] However, to the best of our knowledge,

Received: August 26, 2015
Accepted: September 18, 2015
Published: September 18, 2015

DOI: 10.1021/acsami.5b07895
ACS Appl. Mater. Interfaces 2015, 7, 22719−22726

there have been no reports on the use of any IrO_x applied on a label-free, electrochemical immunosensor for AFP detection.

In this paper, a sensitive, label-free, electrochemical immunosensor for amperometric immunoassay of AFP was designed on the basis of the electrospun IrO_x nanofibers. Especially, the specific wire-in-tube nanostructure of IrO_x nanofibers was first fabricated through a simple one-spinneret electrospinning process. Such IrO_x nanofibers can provide a large effective surface area and act as a rapid electron transfer channel, which make the proposed IrO_x-nanofiber-based immunosensor show good qualities for AFP detection, such as high sensitivity and selectivity, wide detection range, low detection limit, long-term stability, and, moreover, good accuracy to detect AFP in real serum.

2. EXPERIMENTAL SECTION

2.1. Materials and Apparatus. All chemicals used were analytical grade and utilized without further purification. AFP, monoclonal antibody (Ab), carcinoembryonic antigen (CEA), and prostate specific antigen (PSA) were purchased from Beijing Boisynthese Biotechnology Co., Ltd. Bovine serum albumin (BSA) was purchased from Beijing DingGuo Biotechnology Co. Human serum samples were purchased from a local hospital. KH_2PO_4, KCl, Na_2HPO_4, and NaCl were purchased from Beijing Chemical Works. Chitosan (CS) and ascorbic acid (AA) were purchased from Sigam-Aldrich. $IrCl_3$ hydrate (98%) was purchased from Adamas Reagent Co., Ltd. All electrochemical measurements were performed in PBS solution (pH 7.4) containing 5 mM $K_3[Fe(CN)_6]$ on a model CHI660D electrochemical workstation (ChenHua Instruments Co., Ltd., Shanghai, China).

2.2. Electrospinning and Characterization of IrO_x Nanofibers. In our case, different IrO_x nanofibers were obtained through a simple single-spinneret electrospinning process. In a typical process, 0.292 g of $IrCl_3$ was first added into 5 mL of *N*,*N*-dimethylformamide (DMF) solution and stirred a few minutes, then 0.75 g of polyvinylpyrrolidone (PVP; M_w = 1 300 000) was added into the above mixed solution to make the weight ratio of the inorganic salt to PVP ($IrCl_3$/PVP) 0.39. After sufficient stirring, a viscous and clear precursor solution was obtained. Then, the as-prepared precursor solution was added into a plastic syringe (10 mL) for electrospinning. During the electrospinning process, the collecting distance was set as 15 cm between the spinneret tip and the collector, and the applied voltage was 15 kV. After being dried for 12 h at room temperature, the electrospun fibers were annealed in a tube furnace with a heating rate of 1 °C/min from room temperature to 350, 500, 700, or 900 °C for 3 h, and then the furnace self-cooled down to room temperature. The final products were IrO_x nanofibers.

The scanning electron micrographs were obtained with a JEOL JSM-7500F field emission scanning electron microscope (SEM) operating at an accelerating voltage of 15 kV. Transmission electron microscope (TEM) and high-resolution TEM (HR-TEM) images were recorded on a JEM-2010 transmission electron microscope under a working voltage of 200 kV. The crystalline structure of the samples was characterized by X-ray diffraction (XRD) (Rigaku D/max-rA power diffractometer using Cu KR radiation (λ) 1.541 78 Å), and the corresponding lattice constants were calculated by MDI Jade 5.0 software. X-ray photoelectron spectroscopy (XPS) was characterized on an ESCAlab250 Analytical XPL spectrometer with a monochromatic Al KR source, the binding energies of which were referred to the C 1s peak at 284.7 eV of the surface adventitious carbon, and the fitted peaks in XPS spectra were deconvoluted using the XPS Peak 4.1 software. Thermogravimetric analyzer (TGA) data were obtained on a SDT 2960 differential thermal analyzer (TA Instruments, New Castle, DE) with a heating rate of 10 °C/min in air.

2.3. Fabrication of the IrO_x-Modified AFP Immunosensor. For the preparation of the IrO_x-nanofiber-modified AFP immunosensor, the glassy carbon electrode (GCE) was first polished with 1.0, 0.3, and 0.05 μm alumina slurry to a mirrorlike surface, followed by ultrasonic cleaning in dilute nitric acid (0.5 M), acetone, and ethanol, and then the electrodes were dried at room temperature. For better immobilization of the IrO_x nanofibers on the GCE, the IrO_x–CS mixed solutions were prepared by mixing 100 μL of IrO_x solution in water (2 mg/mL) and 50 μL of 1% CS solution by ultrasonic dispersion.[21] Then, 5 μL of different IrO_x–CS mixed solutions were dropped on the surface of the GCE and dried at room temperature. After that, the IrO_x–CS/GCEs were immersed into the AFP-Ab solution (50 μg/mL) for 12 h at 4 °C to immobilize the Ab on the IrO_x–CS/GCEs, then the electrodes were cleaned with distilled water to remove the physically absorbed species. The electrode was incubated in 1% BSA for 1 h at room temperature to block possible active sites. Then the modified electrodes were incubated in different concentrations of AFP solution for 1 h at 37 °C. Finally, the IrO_x-modified AFP immunosensors were obtained and were stored at 4 °C when not in use.

3. RESULTS AND DISCUSSION

3.1. Structure and Morphology of IrO_x Nanofibers. Figure 1a shows the SEM images of the precursor nanofibers

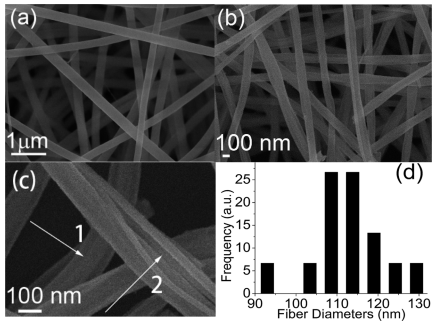

Figure 1. (a) SEM images of the precursor fibers, (b) the IrO_x nanofibers after annealing at 500 °C, and (c) an enlarged SEM image of IrO_x nanofibers after annealing at 500 °C. (d) The corresponding diameter distribution.

before heating treatments. As is displayed, smooth, uniform, long, and continuous composite fibers with an average diameter of ~250 nm are formed. Figure 1b is the SEM image of IrO_x nanofibers after calcination at 500 °C for 3 h. As can be seen, the continuous structure was maintained while the average diameter shrunk to ~110 nm (according to the diameter distribution, as shown in Figure 1d), which might be caused by the decomposition of metal precursor and removal of polymer composition.[22] When the SEM image of the IrO_x nanofibers are further enlarged (Figure 1c), we can observe that a specific wire-in-tube nanostructure is formed, as pointed out by arrows 1 and 2.

In order to provide additional evidence of the formation of a specific nanostructure for the IrO_x nanofibers, TEM analysis was also performed. It can be clearly seen that independent nanowires are embedded in the nanotube and that the wire-in-tube nanostructures possess separated walls along nearly their entire length (Figure 2a). The average diameter of the inside wire and whole nanofiber is ~70 and 110 nm, respectively, and the detailed nanostructure can be observed more clearly in the inset of Figure 2a. Figure 2b shows the HRTEM image and SAED pattern of IrO_x nanofibers. From the HRTEM image, distinct lattice fringes with an interplanar spacing of 0.22 and 0.31 nm can be observed, matching well with the (111) plane of Ir and the (110) plane of IrO_2. The SAED pattern of the IrO_x (inset of Figure 2b) is composed of concentric, alternating dark and bright rings, featuring its polycrystalline nature. To further determine the distribution of Ir and O elements in the

DOI: 10.1021/acsami.5b07895
ACS Appl. Mater. Interfaces 2015, 7, 22719–22726

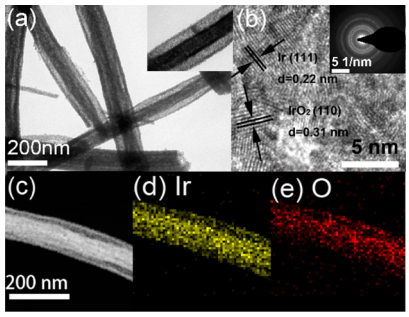

Figure 2. (a) TEM, (b) HRTEM, and (c) STEM images of IrO_x nanofibers after annealing at 500 °C. The inset of panel a is the enlarged TEM image and inset of panel b is the SAED pattern. Panels d and e are the corresponding EDX mapping of Ir and O elements.

IrO_x nanofibers, EDX mapping was conducted. Figure 2c is the corresponding STEM image, which further proves the formation of the specific nanostructure. The distribution of Ir and O elements (Figure 2d,e) is homogeneous and also exhibits a similar wire-in-tube nanostructure, indicating that Ir and IrO_2 are uniformly mixed in the IrO_x nanofibers.

Generally, annealing temperature is an important factor affecting the final morphology of electrospun nanofibers. Accordingly, the TGA curve of $IrCl_3$/PVP composite fibers is applied to monitor the changing process in the view of weight loss. As shown in Figure 3, the weight loss process can be

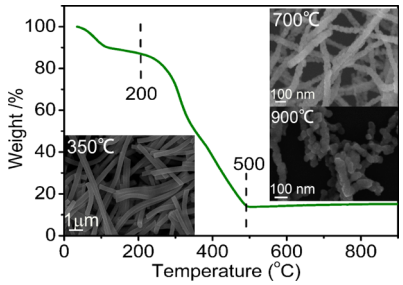

Figure 3. TGA analysis of the $IrCl_3$/PVP fibers, and the insets are the SEM images of the IrO_x nanofibers after annealing at 350, 700, and 900 °C.

divided into two stages. Stage one occurred from 35 to 200 °C, with 13% weight loss, which was attributed to the evaporation of solvent and adsorbed water. The second stage occurred from 200 to 500 °C, associated with 86% weight loss, which mainly originated from the degradation of PVP and the decomposition of metal precursor. At the same time, the crystallites were also formed. Above 500 °C, there was no obvious weight loss, indicating the complete decomposition of PVP. Besides, at this stage, the weight curve of the nanofibers present a slow upward trend (from 13.5% to 15%), indicating that a change of crystal structure may be happened. Moreover, SEM images were collected at different weight loss stages to monitor further the evolution of the morphology. As shown in the insets of the Figure 3, the change of the morphology of the calcination material was obvious with the increase of temperature. At 350 °C, the relative smooth morphology can be maintained, and the average diameter is almost the same as that of precursor $IrCl_3$/PVP nanofibers. This may be owing to the PVP not being completely removed, as proved by the TGA curve. With further increasing the annealing temperature to 700 °C, the wire-in-tube nanostructure disappeared and the nanowire with a rough surface and an average diameter of ~62 nm appeared, indicating the collapse and reunion of the nanofibers. When the temperature was up to 900 °C, the nanowire structure could hardly be maintained and began to break.

Besides, the corresponding XRD patterns were carried out to confirm further the phase characteristics of the nanofibers under different annealing temperatures. As shown in Figure 4a,

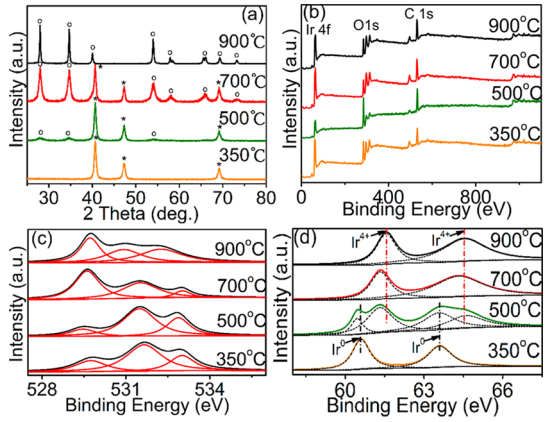

Figure 4. (a) XRD patterns and (b) the complete, (c) O 1s, and (d) Ir 4f XPS spectra of IrO_x nanofibers annealed at 350, 500, 700, and 900 °C.

the diffraction peak for nanofibers obtained under 350 °C can be mainly indexed to the pure monoclinic Ir (JCPDS 46-1044). Along with the increase of the temperature to 500 and 700 °C, the peaks of rutile phase IrO_2 (JCPDS 15-0870) began to appear, and finally, the pure IrO_2 nanofibers were obtained when the temperature was up to 900 °C. This proved that an oxidation process of Ir to IrO_2 occurred from 500 to 900 °C, which is consistent with the TGA curve.

To further confirm the surface composition and element chemical state, XPS spectra of different IrO_x nanofibers were also examined. First, the complete spectra are shown in Figure 4b, which confirm the presence of Ir, O, and C elements. The O 1s XPS spectra of IrO_x nanofibers at different temperatures are enlarged in Figure 4c. The corresponding O 1s core level electrons all display three peaks, with binding energies of ~529.6, 531.3, and 532.7 eV, corresponding to the lattice oxygen in crystalline IrO_2, chemisorbed oxygen, and water-related species, respectively.[20,23] Figure 4d shows the enlarged XPS spectra of Ir 4f. The Ir 4f chemical nature of the IrO_x nanofibers annealed at 350 and 900 °C can be easily assigned to $4f_{5/2}$ (60.6 eV) and $4f_{7/2}$ (63.6 eV) of Ir^0 binding energies and $4f_{5/2}$ (61.5 eV) and $4f_{7/2}$ (64.6 eV) of Ir^{4+} binding energies, respectively. Here, the 4f level of IrO_x nanofibers annealed at 500 °C can be dissolved into two series of peaks composed of Ir^0 and Ir^{4+} binding energies; besides, the peak area of Ir^{4+} seems much larger than that of Ir^0, indicating that the IrO_2 might mainly locate at the surface of IrO_x nanofibers because the surface area is more easily oxidized under high temperature. Moreover, both the binding energies of Ir^0 and Ir^{4+} in IrO_x nanofibers annealed at 500 °C shift to the lower energy side compared to that in IrO_x nanofibers annealed at 350 and 900 °C due to the different local environments and the possible interaction effect between Ir and IrO_2. Also, the decreased binding energies may lead to the enhanced activity of the surface Ir and IrO_2 in IrO_x nanofibers annealed at 500 °C,[24,25] which is very favorable for the following electrochemical

DOI: 10.1021/acsami.5b07895
ACS Appl. Mater. Interfaces 2015, 7, 22719−22726

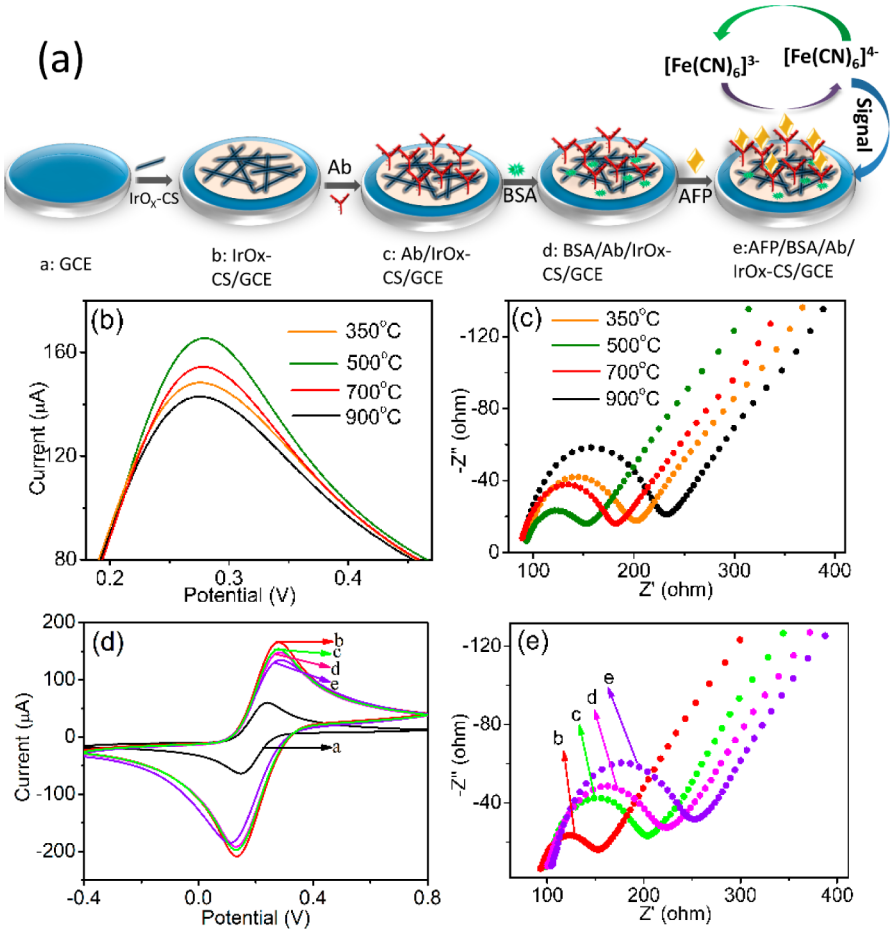

Figure 5. (a) A schematic diagram of the detailed preparation process of an IrO_x-nanofiber-modified immunosensor. (b) CV and (c) EIS spectra of different IrO_x-nanofiber-modified immunosensors. (d) CV and (e) EIS spectra of the fabrication progress of IrO_x-nanofiber-modified (annealed at 500 °C) immunosensor in pH 7.4 PBS solution containing 5.0 mM $[Fe(CN)_6]^{3-/4-}$, where the letters labeling the spectra correspond to the diagram labels in panel a.

detection. For IrO_x nanofibers annealed at 700 °C, the surface area was completely oxidized, as proved by XPS spectrum.

On the basis of the above analysis and some previous studies,[26,27] the formation of the specific IrO_x nanofibers with wire-in-tube structure is proposed. As we know, during electrospinning, the solution jet solidified with the accompanying evaporation of solvent and then formed a nonwoven, fibrous mat on the collector. In this process, because the Ir ions were better dissolved in DMF solution than in PVP, some Ir ions would be carried out to the fiber surface with the solvent evaporation.[28] This effect could be enhanced at elevated environmental temperature,[29] resulting in diffusion of precursor toward the skin and away from the center of the fibers; thus, the nanocrystals migrated closer to the fiber surface. After total decomposition of PVP, particles with small size would collapse to the center of the fiber, whereas the larger particles remain self-supported on the exterior, forming the shell of the loose-tube fibers.[30] Note that the different components (Ir and IrO_2) of nanofiber obtained at 500 °C also assistant the formation of the specific wire-in-tube nanostructure due to the different diffusing rate. Moreover, the existence of a small amount of IrO_2 nanocrystals (as proved by XRD and XPS), which acted as a dopinglike material, may also help to form different-sized nanoparticles. When further increasing the annealing temperature, the nanoparticles tend to agglomerate together, leading to the recombination of the nanostructure.

3.2. Electrochemistry of the Immunosensor.

A schematic illustration of the stepwise self-assembly process of the IrO_x-nanofiber-modified AFP immunosensor appears in Figure 5a. First, the cyclic voltammetry (CV) and electrochemical impedance spectroscopy (EIS) of different IrO_x nanofibers calcined under different temperatures (IrO_x–CS/GCE) were recorded, as shown in Figure 5b,c. Obviously, the peak current of the electrode modified by IrO_x nanofibers treated at 500 °C is the highest one, indicating that those IrO_x nanofibers possess the best electronic conductivity. The relationship for peak currents of different IrO_x-nanofiber-modified electrodes is I(500 °C) > I(700 °C) > I(350 °C) > I(900 °C). In addition, this fact is also consistent with the result of EIS curves in Figure 5c. As can be seen, all the obtained impedance spectra include a semicircle part controlled by the electron-transfer process and a linear part controlled by the diffusion process, and the semicircle diameter equals the electron-transfer resistance (R_{et}). It can be clearly observed that the R_{et} also shows the same changing trend as the peak currents for different IrO_x-nanofiber-modified electrodes. This is because pure Ir has a much better electron transfer rate than IrO_2.[31] In IrO_x nanofibers treated at 500 °C, pure Ir is the main component and the amount of IrO_2 is relatively small (as proved by XRD). While the quantity of IrO_2 gradually increased with the increase of annealing temperature (700 and 900 °C), the electronic transmission gradually decreased.

DOI: 10.1021/acsami.5b07895
ACS Appl. Mater. Interfaces 2015, 7, 22719–22726

Besides, the specific wire-in-tube nanostructure is also very favorable for increasing the electron transfer rate. Note that although the XRD pattern shows that IrO_x nanofibers annealed at 350 °C contain pure Ir, the residual PVP may hinder the electronic transmission (as proved by the TGA curve), resulting in the poor electron-transfer ability.

Accordingly, IrO_x nanofibers (500 °C) were chosen as the best candidate in our case to build an AFP immunosensor. In order to intuitively display the entire fabrication process of the immunosensor, CVs and EIS at each immobilization step were recorded as markers. Figure 5d demonstrates the CVs of different modified electrodes in 5 mM $[Fe(CN)_6]^{3-/4-}$. Compared to the bare GCE (curve a), both the cathodic and anodic peak currents were significantly increased after immobilization with IrO_x nanofibers (500 °C) and chitosan (IrO_x–CS/GCE, curve b), suggesting that IrO_x nanofibers (500 °C) can enhance the conductivity. When the as-modified electrode (IrO_x–CS/GCE) was incubated in the Ab solution for 1 h (Ab/IrO_x–CS/GCE, curve c), the peak current of the electrode showed a decreased trend as a result of the large resistance of Ab, which hindered the electrons' transport. After the additional active sites of the modified electrode were blocked by BSA (BSA/Ab/IrO_x–CS/GCE, curve d), the corresponding peak current was also reduced accordingly. Moreover, after AFP antigen molecules were combined with the antibody molecules, an obvious decrease of the peak currents was obtained (AFP/BSA/Ab/IrO_x–CS/GCE, curve e), indicating that the formed immunocomplex acted as the inert electron- and mass-transfer-blocking layer, hindered the diffusion of ferricyanide toward the electrode surface. All of the obtained results proved that each connection process of the immunsensor is successful.

Besides, the impedance technique was a sensitive and reliable tool for studying the interface properties of the chemically modified electrode surface; thus, EIS was used to further confirm each connection process of the immunosensor. Figure 5e shows the Nyquist plots of the sensing electrode responses with different steps in the assembly process. The significant differences in the impedance spectra during the stepwise modification of the electrodes also can be clearly observed. When IrO_x–CS composites were deposited on the surface of GCE, the diameter of the semicircle was very little, indicating that the film of IrO_x–CS electrode material enhanced the electron transfer process through providing a more conductive medium for the electron transfer. After the modified electrode was incubated in Ab, BSA, and AFP, respectively, the resistance increased gradually as the experiment preceded, which was in good agreement with the CVs results.

The CVs of the prepared IrO_x–CS-modified immunosensor with 10 ng/mL AFP in PBS (pH 7.4) containing 5.0 mM $[Fe(CN)_6]^{3-/4-}$ at various scan rates are shown in Figure 6a. It can be found that the redox peak currents were linearly proportional to the square root of the sweep rate in the range of 10–190 mV/s), illustrating a diffusion-controlled electrochemical process.

3.3. Optimization of Detection Conditions. The pH value of the detection solution is an important factor that great affects the bioactivity of the Ab and antigens. In order to investigate the effect of the pH value on response signal, the IrO_x-nanofiber-modified immunosensor containing 10 ng/mL AFP antigen was incubated in PBS with different pH values at room temperature. As showed in Figure 6b, the peak currents initially increase with an increase of the pH value from 5.0 to 7.4 and then show a decreasing trend. Therefore, PBS with pH value of 7.4 was selected for the further characterization of the immunosensor.

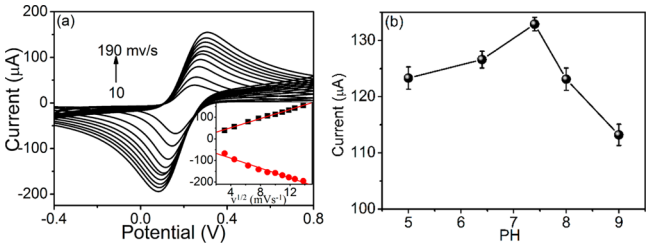

Figure 6. (a) CVs of the IrO_x-nanofiber-modified (annealed at 500 °C) immunosensor with 10 ng/mL AFP in pH 7.4 PBS containing 5.0 mM $[Fe(CN)_6]^{3-/4-}$ at different scan rates of 10, 20, 40, 60, 80, 100, 120, 140, 160, and 190 mV/s, respectively. The inset shows the linear relationship between the peak currents and the square root of the scan rate. (b) The electrochemical behavior of IrO_x-nanofiber-modified (annealed at 500 °C) immunosensor in the pH ranging from 5.0 to 9.0 in PBS solution containing 5 mM $[Fe(CN)_6]^{3-/4-}$.

3.4. Analytical Performance of the Immunosensor. To evaluate the affinity condition between Ab and AFP antigen, the IrO_x-nanofiber-modified immunosensor was exposed to different concentrations of AFP in PBS (PH 7.4) containing 5 mM $[Fe(CN)_6]^{3-/4-}$ to monitor the current response. As showed in Figure 7a, it was obvious that the current response decreased as the AFP concentration increased (0.05–150 ng/mL). This is because with an increasing concentration of antigen (AFP), more antigen–Ab complex forms on the surface of the electrode and further inhibits the electron transfer. Moreover, after exposure to 0.05 ng/mL AFP, the corresponding peak current clearly decreased compared with the unincubated one (inset of Figure 7a). Generally, the concentration of the AFP in normal human serum is less than 10 ng/mL;[32] thus, the as-developed immunosensor could well meet the requirement of practical application in a clinical immunoassay.

The corresponding calibration plot for AFP concentration in PBS (squares) was plotted and at least triplicate analyses were obtained at each concentration using the proposed immunosensor in Figure 7b. As can be seen, the calibration plot exhibits a good linear relationship in the studied range with a detection limit of 20 pg/mL (S/N = 3), and the corresponding calibration equation can be written as Y (μA) = 140.59 − 0.397X (ng/mL), R^2 = 0.9882. Besides, in order to evaluate the applicability of the developed immunosensor to real sample analysis, CV of various concentrations of AFP in human serum was also performed (see Figure S1, Supporting Information), and the corresponding calibration plot (circles) is shown in Figure 7b. Compared to the calibration plot for PBS, the immunosensor also exhibited a good linear relationship in human serum with little slope change [Y (μA) = 133.25 − 0.392X (ng/mL), R^2 = 0.9892], indicating that the as-proposed immunosensor is promising for AFP detection in human serum. However, the current response of the immunosensor in human serum was less than that in PBS, showing the existence of matrix effect of human serum on the response.[33] Table 1 shows a comparison of the IrO_x-nanofiber-modified immunosensor in this work with other noble-metal-modified AFP immunosensors. It can be seen that the linear range of IrO_x-nanofiber-modified immunosensors is satisfactory, with a larger slope, indicating that the as-proposed immunosensor is more sensitive to AFP. Besides, the detection limit of IrO_x-nanofiber-modified

DOI: 10.1021/acsami.5b07895
ACS Appl. Mater. Interfaces 2015, 7, 22719–22726

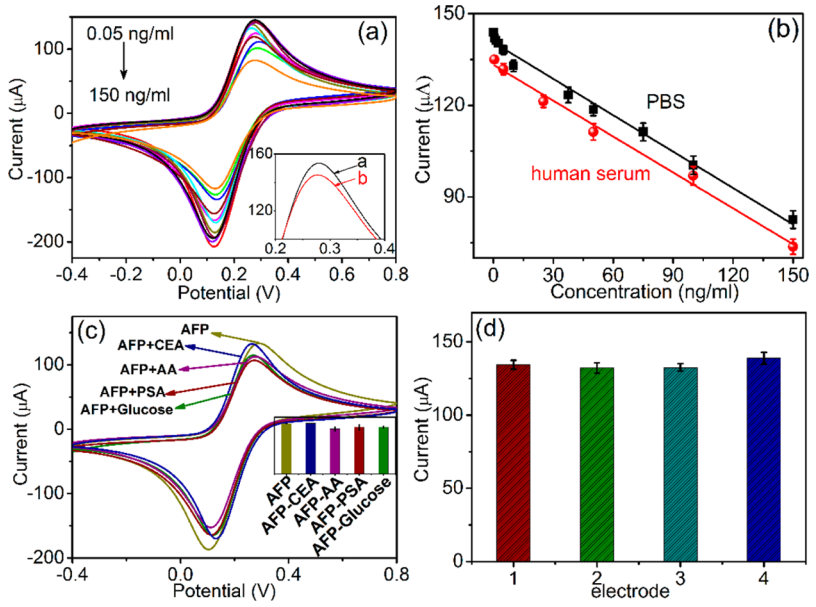

Figure 7. (a) CV of IrO_x-nanofiber-modified (annealed at 500 °C) immunosensor responded to different concentrations of AFP. (b) The calibration curves of the response of the immunosensor used in panel a to different concentrations of AFP in PBS and human serum. (c) The specificity of IrO_x-nanofiber-modified (annealed at 500 °C) immunosensor toward AFP, AFP + CEA, AFP + PSA, AFP + AA, and AFP + glucose; the inset is the corresponding response histogram. (d) The reproducibility of IrO_x-nanofiber-modified (annealed at 500 °C) immunosensor toward different electrodes.

Table 1. A Comparison of Analytical Properties of the as-Developed Immunosensor with Other AFP Immunosensors

materials[a]	linear range	detection limit	refs
IrO_x/chitosan	0.05−150 ng/mL	20 pg/mL	this work
gold nanomushroom arrays	20−200 ng/mL	24 ng/mL	34
graphene/Au−Pd	0.05−30 ng/mL	0.005 ng/mL	35
AuNPs−Ab/AFP/Ab−HRP sandwich	5−80 ng/mL	3.7 ng/mL	36
Pd−rGO	0.01−12 ng/mL	5 pg/mL	37
Au NWs/ZnO NRs	0.5−160 ng/mL	0.1 ng/mL	38
collagen−TiO_2/nano-Au	0.10−60 ng/mL	29 pg/mL	39
HRP−MPS/PVA/ITO	1−90 ng/mL	0.5 ng/mL	40

[a]Abbreviations: NPs = nanoparticles, HRP = horseradish peroxidase, NWs = nanowires, NRs = nanorods. MPS = mesoporous silica, PVA = poly(vinyl alcohol).

immunosensors was much lower than that of other immunosensors, except the graphene/Au−Pd-modified immunosensor and Pd−reduced graphene oxide (rGO), which showed a lower limit. However, graphene/Au−Pd-modified immunosensor and Pd−rGO had a much narrower linear range. The good electrochemical performance of the IrO_x-nanofiber-modified immunosensor can be mainly attributed to the IrO_x nanofibers possessing good electron transfer nature and specific wire-in-tube nanostructure, which can provide a good microenvironment for immobilizing the Ab and AFP antigen and then greatly enhance the electrochemical signal.

3.5. Selectivity, Reproducibility, and Stability. A selectivity test was performed in order to evaluate the interference immunity of an IrO_x-nanofiber-modified immunosensor. The immunosensor was first incubated with (10 ng/mL) in the presence of other interfering agents, which potentially coexisted with AFP in human serum. As shown in in Figure 7c, the change of current response caused by interfering substances was less than 10% compared to that of pure AFP, and even the concentration of the interfering agents was 10-fold that of AFP, illustrating the high selectivity of the as-proposed immunosensor.

Reliability is an important factor to judge the performance of an immunosensor. Here, the reproducibility was investigated through analyzing the current response of four equally prepared immunosensors with the same concentration of AFP (10 ng/mL). As shown in Figure 7d, the relative standard deviation was less than 5%. The stability of the immunosensor was obtained through checking their current responses every week, and the immunosensor was stored at 4 °C when not in use. After 6 days, the current response of the immunosensor had a change of 8.7%. After 15 days, the current response retained 14% of its initial current, suggesting a good stability of the immunosensors.

4. CONCLUSIONS

In this work, IrO_x nanofibers have been successfully synthesized by using a typical electrospinning method. The specific wire-in-tube nanostructure can be easily obtained through simply controlling the annealing temperature, where the crystalline phase also could be simultaneously changed. Compared to the other IrO_x nanofibers with different morphology and crystalline phase, the IrO_x nanofibers annealed at 500 °C, with specific wire-in-tube nanostructure and Ir/IrO_2 phase, greatly improved

DOI: 10.1021/acsami.5b07895
ACS Appl. Mater. Interfaces 2015, 7, 22719−22726

the electronic transmission rate and enhanced the electrochemical signal and stability of the immunosensor for the diagnosis of AFP, because of its unique structure, electrical conductivity, high chemical activity, high electroactive surface area, and thermal stability. Besides, the proposed immunosensor also exhibited excellent performance for the clinical detection of AFP, with simple operation, good selectivity, and long-term stability. The IrO_x-nanofiber-modified immnuosensor is stable, versatile, and reproducible, which can be further developed for other immunoassays.

■ ASSOCIATED CONTENT

Supporting Information

The Supporting Information is available free of charge on the ACS Publications website at DOI: 10.1021/acsami.5b07895.

The CVs of the IrO_x-nanofiber-modified (annealed at 500 °C) immunosensor at different concentrations of AFP in human serum (Figure S1) (PDF)

■ AUTHOR INFORMATION

Corresponding Authors

*L.X.: e-mail, linxu@jlu.edu.cn; tel, 86-431-81736604.
*H.S.: e-mail, songhw@jlu.edu.cn; tel, 86-431-81736614.

Notes

The authors declare no competing financial interest.

■ ACKNOWLEDGMENTS

This work was supported by NSFC (Grant Nos. 61204015, 81301289, 61177042), Program for Chang Jiang Scholars and Innovative Research Team in University (No. IRT13018), The Jilin Province Natural Science Foundation of China (Nos. 20150520090JH, 20140101171JC), Jilin Provincial Economic Structure Strategic Adjustment Fund Special Projects (No. 2014Y082), and Project 2015021 supported by Graduate Innovation Fund of Jilin University.

■ REFERENCES

(1) Cui, H.; Hong, C.; Ying, A.; Yang, X.; Ren, S. Ultrathin Gold Nanowire-Functionalized Carbon Nanotubes for Hybrid Molecular Sensing. *ACS Nano* **2013**, *7* (9), 7805−7811.

(2) Su, B.; Tang, D.; Li, Q.; Tang, J.; Chen, G. Gold-Silver-Graphene Hybrid Nanosheets-Based Sensors for Sensitive Amperometric Immunoassay of Alpha-fetoprotein Using Nanogold-Enclosed Titania Nanoparticles as Labels. *Anal. Chim. Acta* **2011**, *692* (1−2), 116−124.

(3) Zhou, C.; Liu, D.; Xu, L.; Li, Q.; Song, J.; Xu, S.; Xing, R.; Song, H. A Sensitive Label-Free Amperometric Immunosensor for Alpha-fetoprotein Based on Gold Nanorods with Different Aspect Ratio. *Sci. Rep.* **2015**, *5*, 9939.

(4) Chen, M.-J.; Wu, Y.-S.; Lin, G.-F.; Hou, J.-Y.; Li, M.; Liu, T.-C. Quantum-Dot-Based Homogeneous Time-Resolved Fluoroimmunoassay of Alpha-fetoprotein. *Anal. Chim. Acta* **2012**, *741*, 100−105.

(5) Darwish, I. A.; Wani, T. A.; Alanazi, A. M.; Hamidaddin, M. A.; Zargar, S. Kinetic-Exclusion Analysis-Based Immunosensors Versus Enzyme-Linked Immunosorbent Assays for Measurement of Cancer Markers in Biological Specimens. *Talanta* **2013**, *111*, 13−19.

(6) Law, W.-C.; Yong, K.-T.; Baev, A.; Prasad, P. N. Sensitivity Improved Surface Plasmon Resonance Biosensor for Cancer Biomarker Detection Based on Plasmonic Enhancement. *ACS Nano* **2011**, *5* (6), 4858−4864.

(7) Xiao, F.-N.; Wang, M.; Wang, F.-B.; Xia, X.-H. Graphene-Ruthenium(II) Complex Composites for Sensitive ECL Immunosensors. *Small* **2014**, *10* (4), 706−716.

(8) Kavosi, B.; Hallaj, R.; Teymourian, H.; Salimi, A. Au Nanoparticles/PAMAM Dendrimer Functionalized Wired Ethylene-amine-Viologen as Highly Efficient Interface for Ultra-Sensitive Alpha-fetoprotein Electrochemical Immunosensor. *Biosens. Bioelectron.* **2014**, *59*, 389−396.

(9) Wang, G.-L.; Xu, J.-J.; Chen, H.-Y.; Fu, S.-Z. Label-Free Photoelectrochemical Immunoassay for Alpha-fetoprotein Detection Based on TiO2/CdS Hybrid. *Biosens. Bioelectron.* **2009**, *25* (4), 791−796.

(10) Wang, H.; Li, H.; Zhang, Y.; Wei, Q.; Ma, H.; Wu, D.; Li, Y.; Zhang, Y.; Du, B. Label-Free Immunosensor Based on Pd Nanoplates for Amperometric Immunoassay of Alpha-fetoprotein. *Biosens. Bioelectron.* **2014**, *53*, 305−309.

(11) Ding, Y.; Wang, Y.; Li, B.; Lei, Y. Electrospun Hemoglobin Microbelts Based Biosensor for Sensitive Detection of Hydrogen Peroxide and Nitrite. *Biosens. Bioelectron.* **2010**, *25* (9), 2009−2015.

(12) Liang, R.-P.; Wang, Z.-X.; Zhang, L.; Qiu, J.-D. A Label-Free Amperometric Immunosensor for Alpha-fetoprotein Determination Based on Highly Ordered Porous Multi-Walled Carbon Nanotubes/Silica Nanoparticles Array Platform. *Sens. Actuators, B* **2012**, *166-167*, 569−575.

(13) Song, J.; Xu, L.; Xing, R.; Qin, W.; Dai, Q.; Song, H. Ag Nanoparticles Coated NiO Nanowires Hierarchical Nanocomposites Electrode for Nonenzymatic Glucose Biosensing. *Sens. Actuators, B* **2013**, *182*, 675−681.

(14) Wang, L.; Hou, Z.; Quan, Z.; Li, C.; Yang, J.; Lian, H.; Yang, P.; Lin, J. One-Dimensional Ce3+- and/or Tb3+-Doped X-1-Y2SiO5 Nanofibers and Microbelts: Electrospinning Preparation and Luminescent Properties. *Inorg. Chem.* **2009**, *48* (14), 6731−6739.

(15) Hou, Z.; Li, X.; Li, C.; Dai, Y.; Ma, P. a.; Zhang, X.; Kang, X.; Cheng, Z.; Lin, J. Electrospun Upconversion Composite Fibers as Dual Drugs Delivery System with Individual Release Properties. *Langmuir* **2013**, *29* (30), 9473−9482.

(16) Zhao, X.; Cai, B.; Tang, Q.; Tong, Y.; Liu, Y. One-Dimensional Nanostructure Field-Effect Sensors for Gas Detection. *Sensors* **2014**, *14* (8), 13999−14020.

(17) Rivas, L.; Mayorga-Martinez, C. C.; Quesada-Gonzalez, D.; Zamora-Galvez, A.; de la Escosura-Muniz, A.; Merkoci, A. Label-Free Impedimetric Aptasensor for Ochratoxin-A Detection Using Iridium Oxide Nanoparticles. *Anal. Chem.* **2015**, *87* (10), 5167−5172.

(18) Smith, R. D. L.; Sporinova, B.; Fagan, R. D.; Trudel, S.; Berlinguette, C. P. Facile Photochemical Preparation of Amorphous Iridium Oxide Films for Water Oxidation Catalysis. *Chem. Mater.* **2014**, *26* (4), 1654−1659.

(19) Kim, S.-j.; Kim, Y. L.; Yu, A.; Lee, J.; Lee, S. C.; Lee, C.; Kim, M. H.; Lee, Y. Electrospun Iridium Oxide Nanofibers for Direct Selective Electrochemical Detection of Ascorbic Acid. *Sens. Actuators, B* **2014**, *196*, 480−488.

(20) Zhao, C.; Yu, H.; Li, Y.; Li, X.; Ding, L.; Fan, L. Electrochemical Controlled Synthesis and Characterization of Well-Aligned IrO2 Nanotube Arrays With Enhanced Electrocatalytic Activity Toward Oxygen Evolution Reaction. *J. Electroanal. Chem.* **2013**, *688*, 269−274.

(21) Dai, H.; Xu, G.; Zhang, S.; Gong, L.; Li, X.; Yang, C.; Lin, Y.; Chen, J.; Chen, G. Carbon Nanotubes Functionalized Electrospun Nanofibers Formed 3D Electrode Enables Highly Strong ECL of Peroxydisulfate and Its Application in Immunoassay. *Biosens. Bioelectron.* **2014**, *61*, 575−578.

(22) Xu, L.; Dong, B.; Wang, Y.; Bai, X.; Liu, Q.; Song, H. Electrospinning Preparation and Room Temperature Gas Sensing Properties of Porous In2O3 Nanotubes and Nanowires. *Sens. Actuators, B* **2010**, *147* (2), 531−538.

(23) Xing, R.; Xu, L.; Song, J.; Zhou, C.; Li, Q.; Liu, D.; Song, H. W. Preparation and Gas Sensing Properties of In2O3/Au Nanorods for Detection of Volatile Organic Compounds in Exhaled Breath. *Sci. Rep.* **2015**, *5*, 10717.

(24) Xu, L.; Xing, R.; Song, J.; Xu, W.; Song, H. ZnO-SnO2 Nanotubes Surface Engineered by Ag Nanoparticles: Synthesis, Characterization, and Highly Enhanced HCHO Gas Sensing Properties. *J. Mater. Chem. C* **2013**, *1* (11), 2174−2182.

DOI: 10.1021/acsami.5b07895
ACS Appl. Mater. Interfaces 2015, 7, 22719−22726

(25) Zheng, Y.; Zheng, L.; Zhan, Y.; Lin, X.; Zheng, Q.; Wei, K. Ag/ZnO Heterostructure Nanocrystals: Synthesis, Characterization, and Photocatalysis. *Inorg. Chem.* **2007**, *46* (17), 6980−6986.
(26) Fu, J.; Zhang, J.; Peng, Y.; Zhao, C.; He, Y.; Zhang, Z.; Pan, X.; Mellors, N. J.; Xie, E. Wire-in-Tube Structure Fabricated by Single Capillary Electrospinning Via Nanoscale Kirkendall Effect: The Case of Nickel-Zinc Ferrite. *Nanoscale* **2013**, *5* (24), 12551−12557.
(27) Wu, J.; Wang, N.; Zhao, Y.; Jiang, L. Electrospinning of Multilevel Structured Functional Micro-/Nanofibers and Their Applications. *J. Mater. Chem. A* **2013**, *1* (25), 7290−7305.
(28) Wu, J.; Zeng, D.; Wang, X.; Zeng, L.; Huang, Q.; Tang, G.; Xie, C. Mechanistic Insights into Formation of SnO2 Nanotubes: Asynchronous Decomposition of Poly(vinylpyrrolidone) in Electrospun Fibers during Calcining Process. *Langmuir* **2014**, *30* (37), 11183−11189.
(29) Lu, B.; Zhu, C.; Zhang, Z.; Lan, W.; Xie, E. Preparation of Highly Porous TiO2 Nanotubes and Their Catalytic Applications. *J. Mater. Chem.* **2012**, *22* (4), 1375−1379.
(30) Cavaliere, S.; Subianto, S.; Savych, I.; Tillard, M.; Jones, D. J.; Roziere, J. Dopant-Driven Nanostructured Loose-Tube SnO2 Architectures: Alternative Electrocatalyst Supports for Proton Exchange Membrane Fuel Cells. *J. Phys. Chem. C* **2013**, *117* (36), 18298−18307.
(31) Ma, D. L.; Chen, H. L. Use of Simple Annealing Processes to Prepare Anisotropic Iridium and Iridium Dioxide Nanostructures. *CrystEngComm* **2011**, *13* (7), 2779−2784.
(32) Yuan, Y.; Yuan, R.; Chai, Y.; Zhuo, Y.; Shi, Y.; He, X.; Miao, X. Reagentless Amperometric Immunosensor for Alpha-fetoprotein Based on Gold Nanoparticles/TiO2 Colloids/Prussian Blue Modified Platinum Electrode. *Electroanalysis* **2007**, *19* (13), 1402−1410.
(33) Parshetti, G. K.; Lin, F.-h.; Doong, R.-a. Sensitive Amperometric Immunosensor for Alpha-fetoprotein Detection Based on Multifunctional Dumbbell-Like Au-Fe3O4 Heterostructures. *Sens. Actuators, B* **2013**, *186*, 34−43.
(34) Li, W.; Jiang, X.; Xue, J.; Zhou, Z.; Zhou, J. Antibody Modified Hold Nano-Mushroom Arrays for Rapid Detection of Alpha-fetoprotein. *Biosens. Bioelectron.* **2015**, *68*, 468−474.
(35) Zhao, L.; Li, S.; He, J.; Tian, G.; Wei, Q.; Li, H. Enzyme-Free Electrochemical Immunosensor Configured With Au-Pd Nanocrystals and N-doped Graphene Sheets for Sensitive Detection of AFP. *Biosens. Bioelectron.* **2013**, *49*, 222−225.
(36) Giannetto, M.; Elviri, L.; Careri, M.; Mangia, A.; Mori, G. A Voltammetric Immunosensor Based on Nanobiocomposite Materials for the Determination of Alpha-fetoprotein in Serum. *Biosens. Bioelectron.* **2011**, *26* (5), 2232−2236.
(37) Qi, T.; Liao, J.; Li, Y.; Peng, J.; Li, W.; Chu, B.; Li, H.; Wei, Y.; Qian, Z. Label-Free Alpha fetoprotein Immunosensor Established by the Facile Synthesis of a Palladium-Graphene Nanocomposite. *Biosens. Bioelectron.* **2014**, *61*, 245−250.
(38) Lu, X.; Bai, H.; He, P.; Cha, Y.; Yang, G.; Tan, L.; Yang, Y. A Reagentless Amperometric Immunosensor for Alpha-1-fetoprotein Based on Gold Nanowires and ZnO Nanorods Modified Electrode. *Anal. Chim. Acta* **2008**, *615* (2), 158−164.
(39) Su, H.; Yuan, R.; Chai, Y.; Zhuo, Y. Enzyme-Nanoparticle Conjugates at Oil-Water Interface for Amplification of Electrochemical Immunosensing. *Biosens. Bioelectron.* **2012**, *33* (1), 288−292.
(40) Lin, J.; Wei, Z.; Mao, C. A Label-Free Immunosensor Based on Modified Mesoporous Silica for Simultaneous Determination of Tumor Markers. *Biosens. Bioelectron.* **2011**, *29* (1), 40−45.

DOI: 10.1021/acsami.5b07895
ACS Appl. Mater. Interfaces 2015, 7, 22719−22726